RSC Advances

PAPER

View Article Online
View Journal | View Issue

Cite this: *RSC Adv.*, 2024, **14**, 26219

A novel green and efficient heterogeneous acid catalyst for the one-pot synthesis of benzopyrazine-aminoimidazole hybrids with antiproliferative potential †

Ali Altharawi, *[a] Safar M. Alqahtani,[a] Taibah Aldakhil,[a] Pawan Sharma,[bc] Abhishek Kumar[de] and Montather F. Ramadan[f]

A novel, green, efficient, and stable magnetically heterogeneous nanocatalyst was developed by immobilizing butanesulfonic acid ($BuSO_3H$) onto the surface of MFe_2O_4 magnetic nanoparticles (MNPs). The resulting core–shell structure of the MFe_2O_4@PDA@$BuSO_3H$ nanocatalyst was thoroughly characterized using various analytical techniques, including Fourier-Transform Infrared Spectroscopy (FT-IR), X-ray Diffraction (XRD), Energy-Dispersive X-ray Spectroscopy (EDS), Field Emission Scanning Electron Microscopy (FESEM), Transmission Electron Microscopy (TEM), Vibrating Sample Magnetometry (VSM), and Brunauer–Emmett–Teller (BET) analysis. A nanocatalyst was used to synthesize 2-benzopyrazine-aminoimidazole hybrid derivatives through a domino multicomponent Knoevenagel–condensation–cyclization reaction (**5a–p**) in an environmentally friendly manner. The resulting compounds were then tested for their anticancer activity against three types of human cancer cells (MCF-7, A549, and U87) using the MTT assay. The experiment showed that the nanocatalyst had excellent catalytic activity, and the synthesized compounds exhibited promising antiproliferative activity. Notably, compounds **5g** and **5h**, containing a 2-naphthyl ring, showed the highest antiproliferative effects against MCF-7 cells, with IC_{50} values of 0.03 and 0.32 μM, respectively. Additionally, the activity of compounds **5g** and **5h** in tubulin polymerization, apoptosis induction, and cell cycle arrest in MCF-7 cells were investigated. The results demonstrated that these compounds effectively induced apoptosis and cell cycle arrest. The binding of representative compounds to the colchicine binding site of tubulin was confirmed through molecular modeling studies.

Received 29th June 2024
Accepted 12th August 2024

DOI: 10.1039/d4ra04725g

rsc.li/rsc-advances

1. Introduction

Benzopyrazine (quinoxaline), a heteroaromatic ring containing nitrogen, is a bioisostere of privileged functional scaffolds such as benzimidazole, benzothiophene, and quinoline.[1] It has been found to possess diverse biological and therapeutic applications, displaying potential anticancer properties *via* multiple mechanisms, including inhibition of kinase, tubulin polymerization, and topoisomerase.[2–4] Synthetic derivatives of benzopyrazine, particularly those containing 2-amino benzopyrazine, have shown significant medicinal roles as antiproliferative agents, particularly by inhibiting tubulin polymerization. For instance, Alanazi *et al.* synthesized a new set of benzopyrazine-based derivatives with anticancer and VEGFR-2 inhibitory properties.[5] Compound **1** (Fig. 1) is highly effective against HepG2 and MCF-7 cell lines, with IC_{50} values of 12.9 μM and 7.5 μM. In another study, a series of novel derivatives based on triazole benzopyrazine were designed and synthesized as inhibitors of VEGFR-2. Among these derivatives, Compound **2** (Fig. 1) has exhibited the most promising cytotoxic effect against HepG2 and MCF-7cell lines, with IC_{50} values of 4.9 μM and 6.2 μM, in comparison to sorafenib (which shows IC_{50} values of 3.53 μM and 2.18 μM against these cell lines).[6] It is worth noting that these are novel findings and contribute to developing new potential anticancer agents.

The incorporation of an appropriate motif in drug discovery is crucial for generating new medicinal structures that have the potential to act as bioactive agents targeting specific sites. 2-

[a]*Department of Pharmaceutical Chemistry, College of Pharmacy, Prince Sattam Bin Abdulaziz University, Al-Kharj 11942, Saudi Arabia. E-mail: a.altharawi@psau.edu.sa*
[b]*Department of Chemistry, School of Sciences, Jain (Deemed-to-be) University, Bengaluru, Karnataka 560069, India*
[c]*Department of Sciences, Vivekananda Global University, Jaipur, Rajasthan 303012, India*
[d]*School of Pharmacy-Adarsh Vijendra Institute of Pharmaceutical Sciences, Shobhit University, Gangoh, Uttar Pradesh 247341, India*
[e]*Department of Pharmacy, Arka Jain University, Jamshedpur, Jharkhand 831001, India*
[f]*College of Dentistry, Al-Ayen University, Thi-Qar, Iraq*

† Electronic supplementary information (ESI) available. See DOI: https://doi.org/10.1039/d4ra04725g

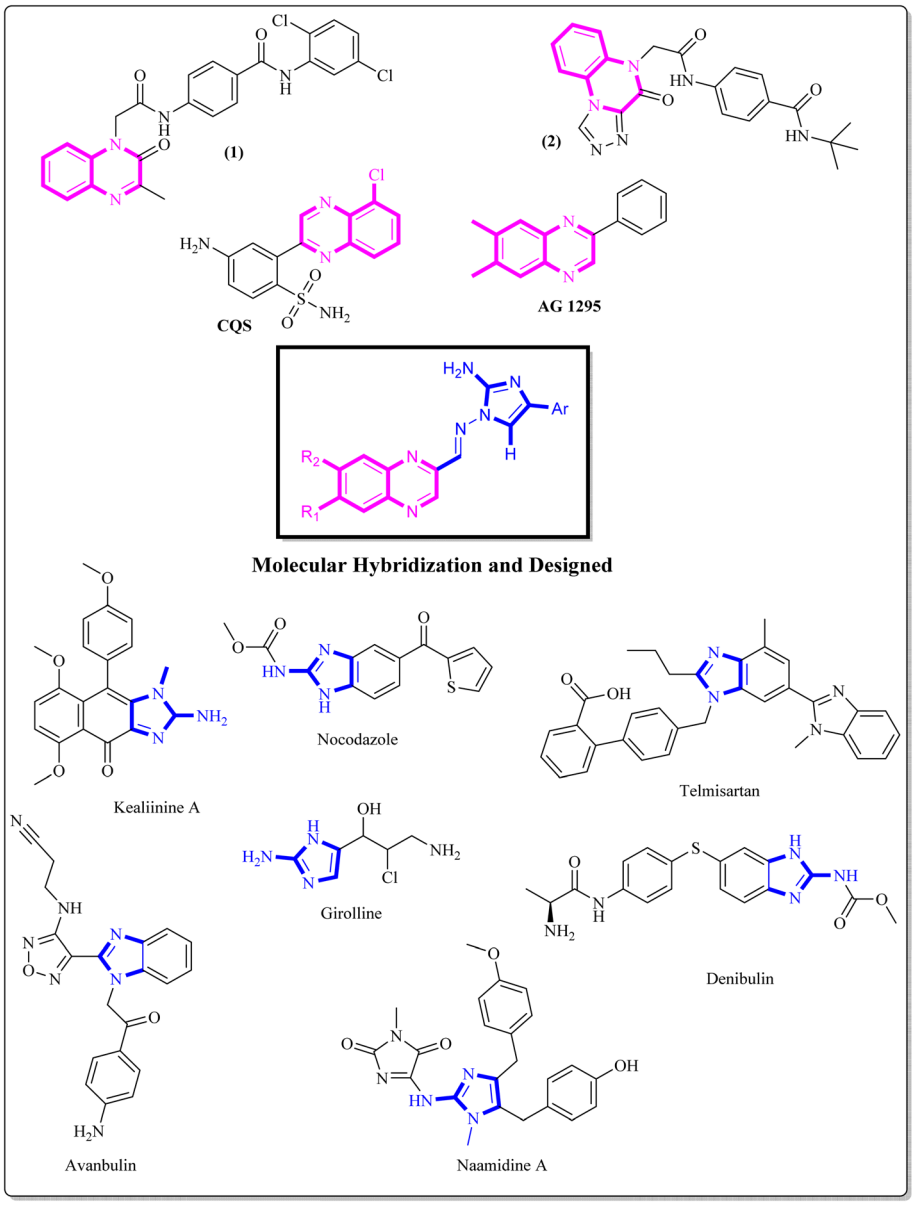

Fig. 1 Some benzopyrazine-based drug-like candidates and benzopyrazine-derived synthetic compounds.

Aminoimidazole, a heterocyclic scaffold, is highly valuable and has wide-ranging applications in various fields, especially as a therapeutic/bioactive agent.[7] It exhibits an exciting pattern of hydrogen bond donation and acceptance during target interactions. Numerous studies have highlighted the anticancer properties of benzimidazole derivatives. Denibulin, nocodazole, and avanbulin (Fig. 1) are benzimidazole-based anticancer drugs that exert their effects by inhibiting tubulin polymerization.[7–9]

Extensive research has been conducted on the anticancer properties of molecules that contain *N*-benzylated benzimidazoles. Telmisartan G, a representative antihypertensive drug bearing an *N*-benzylated benzimidazole core, has been reported for its anticancer activity.[8] Additionally, the synergistic activity of LLS30 H, a derivative of *N*-benzylated benzimidazole, which is a hybrid with docetaxel, has been reported by Tsung-Chieh Shih *et al.* Based on the results, these compounds effectively inhibited the growth and metastasis of prostate cancer cells *in vivo*.[9,10]

Despite developing various synthetic methods for highly functionalized 2-aminoimidazole and benzopyrazine core moieties, driven by the increasing demand for natural product synthesis and medicinal chemistry, most of these methods contain lengthy experimental procedures steps.[11–13] Furthermore, while numerous protocols have demonstrated advantages, they also possess limitations such as extended reaction durations, toxic and costly reagent requirements, and challenges in separating and recycling catalysts.[14–17] Therefore, there is a pressing need to explore sustainable and environmentally friendly protocols and efficient and reusable catalysts to prepare

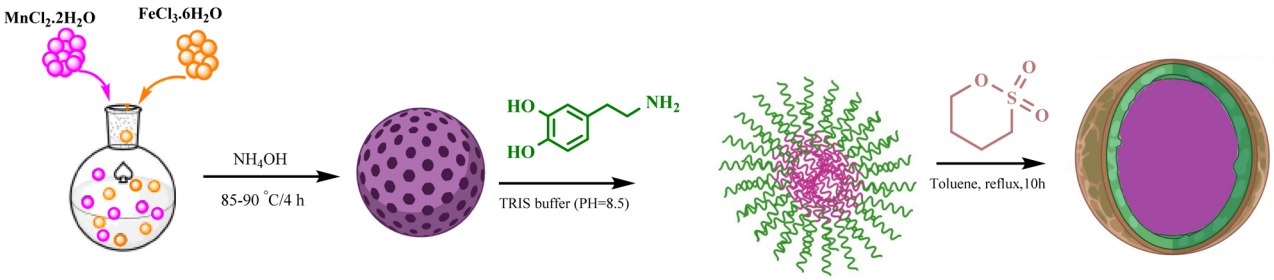

Scheme 1 Synthesis of MFe_2O_4@PDA@ $BuSO_3H$ MNPs as a new heterogeneous catalyst.

benzopyrazine and 2-aminoimidazole motifs. This is a significant challenge associated with ongoing research.

In recent years, nano heterogeneous acid catalysts have been emerging as effective tools for synthesizing bioactive molecules due to their high surface area and the ability to provide a high density of active sites. These catalysts have not only improved catalytic efficiency but also facilitated greener chemical processes.[16,17] Magnetically recoverable nano-catalysts, in particular, offer the dual benefits of easy separation and reusability, making them highly attractive for sustainable chemistry.[18,19]

In this work, we report a rapid, highly efficient, and environmentally benign synthetic pathway for the preparation of a leak-free, high-performance, and stably attached heterogeneous magnetic nanocatalyst, achieved by grafting sulfonic groups onto the surface of dopamine-coated MNPs.[18–22] The polydopamine (PDA) coating on the MNPs endows them with exceptional adhesion properties and outstanding biocompatibility. The surface of these particles can be further modified due to the presence of abundant carboxyl and amino groups. PDA serves as a bridge connecting two functional heads through its amino and quinone groups, which form Schiff base addition adducts *via* the oxidation of dopamine. This bridging capability results in a strong affinity for the hydroxyl and NH groups on the surface of MFe_2O_4@PDA MNPs. Consequently, it facilitates the grafting of $BuSO_3H$ functionalities, as depicted in Scheme 1. Following the successful synthesis of the organic–inorganic framework MFe_2O_4@PDA@$BuSO_3H$ MNPs, its effectiveness as a core–shell-structured nanocatalyst in the multicomponent one-pot cascade synthesis of a novel series of benzopyrazine derivatives containing 2-aminoimidazole was evaluated. Additionally, in line with the rationale guiding the design of these hybrid ligands, molecular docking simulations focused on the colchicine binding site of tubulin were utilized to investigate the mechanisms underlying their notable anti-proliferative activities.

2. Results and discussion

2.1. Chemistry

2.1.1. Synthesis and characterization of MFe_2O_4@PDA@$BuSO_3H$ catalyst. Nanomagnetic particles MFe_2O_4 were obtained from the reaction of iron(III) chloride hexahydrate (0.541 g, 2 mmol) and manganese(II) chloride (0.113 g, 0.7 mmol) in ammonia solution with minor modifications. Subsequently, the surfaces were coated with PDA through the oxidative polymerization of dopamine under primary conditions (Scheme 1). The next step involved functionalizing the amine groups on the surface of the magnetic nanoparticles with $BuSO_3H$ to produce the nanocatalyst. The structural properties of the magnetically heterogeneous nanocatalyst were identified using a variety of analytical techniques, including Fourier-Transform Infrared Spectroscopy (FT-IR), X-ray Diffraction (XRD), Energy-Dispersive X-ray Spectroscopy (EDS), Field Emission Scanning Electron Microscopy (FESEM), Transmission Electron Microscopy (TEM), Vibrating Sample Magnetometry (VSM), and Brunauer–Emmett–Teller (BET) analysis. The FTIR spectrum of the resulting MNPs shows characteristic peaks for PDA at 1430–1610 cm^{-1}, confirming the successful functionalization of the magnetic nanoparticles with PDA polymer (Fig. 2A). The peak at 2931 cm^{-1} corresponds to the C–H stretching vibrations of alkyl groups, while the broad peak at 3442 cm^{-1} is attributed to the SO_3H groups.

The XRD pattern of the uncoated MNPs is consistent with that of spinel ferrites (Fig. 2B). All peaks' positions and relative intensities match the standard XRD pattern of Fe_2O_3 MNPs (JCPDS card no. 85-1436), indicating that the MNPs retain their crystalline cubic spinel structure. The XRD patterns of the particles exhibit nine characteristic peaks associated with a cubic iron oxide phase (2θ = 14.80°, 30.10°, 35.50°, 43.10°, 53.00°, 57.00°, 62.80°, 70.50°, 73.90°), which are indexed as (1 1 0), (2 2 0), (3 1 1), (4 0 0), (3 3 1), (4 2 2), (5 1 1), (4 4 0), and (5 3 1), respectively. Based on the XRD pattern data and the Scherrer equation, the crystalline size of MFe_2O_4@PDA@$BuSO_3H$ MNPs is estimated to be 30 nm.

The BET method is essential in determining materials' specific surface area (SSA). To calculate the average particle diameter (nm), the following formula can be utilized: dBET = $6000/(\rho s \times S)$, where S represents the specific surface area in m^2 g^{-1}, and ρ is the theoretical density in g cm^{-3}.[21,23] During the measurement of surface area, when solid particles are not agglomerated, nitrogen gas (N_2) permeates the pores and surfaces of the powder, as illustrated in Fig. 2C.

To assess the magnetic characteristics of MFe_2O_4@PDA@$BuSO_3H$, a VSM was used at room temperature under an applied field of approximately 10 000 Oe. As shown in Fig. 2D, the saturation magnetization (M_s) values for MFe_2O_4@ and MFe_2O_4@PDA@$BuSO_3H$ catalysts are about 67 emu g^{-1} and 55

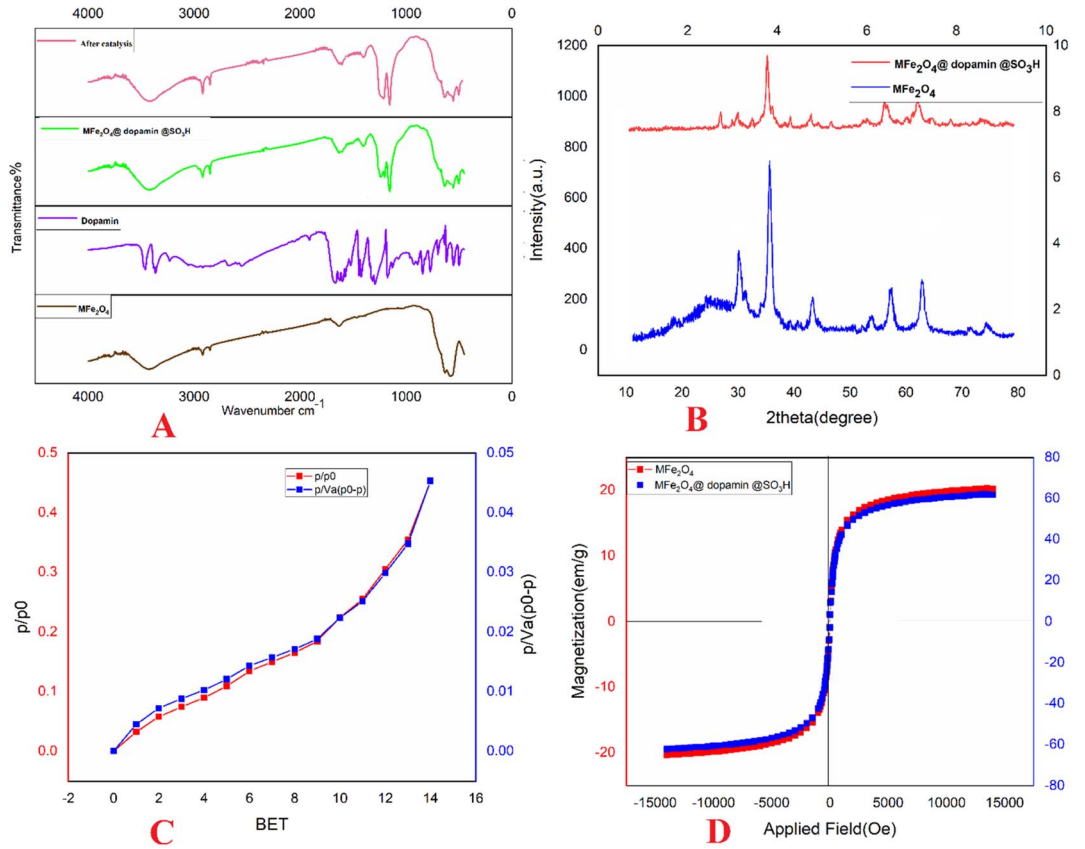

Fig. 2 FT-IR spectra (A); XRD spectra (B); BET (C) and VSM (D) diagrams of MFe_2O_4@PDA@BuSO_3H MNPs.

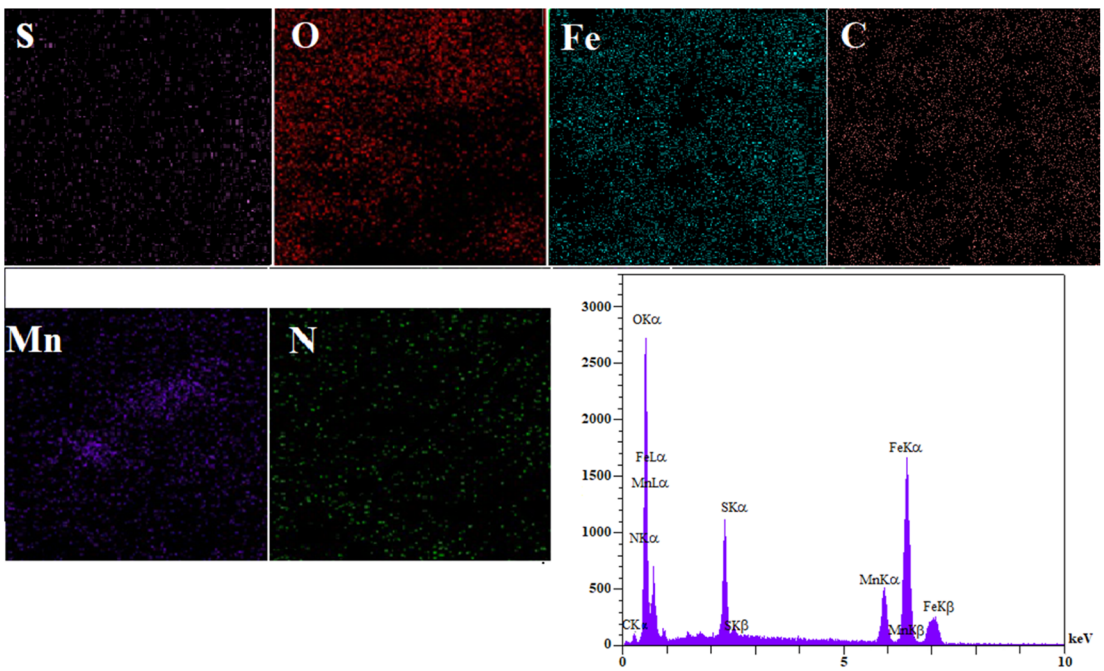

Fig. 3 EDS spectra of MFe_2O_4@PDA@BuSO_3H MNPs.

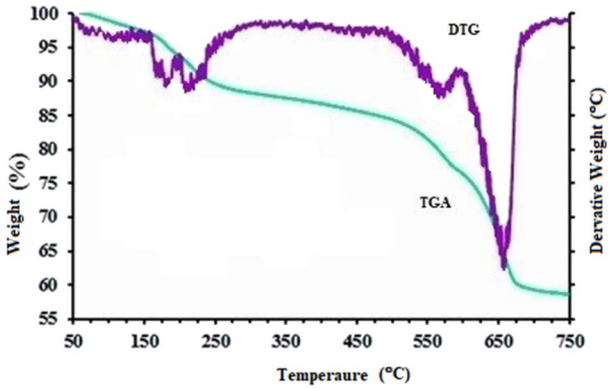

Fig. 4 TGA spectra of MFe_2O_4@PDA@$BuSO_3H$ MNPs.

emu g^{-1}, respectively. Compared to uncoated MFe_2O_4 MNPs (67.22 emu g^{-1}), the saturation magnetization of the coated catalysts exhibited a significant decrease due to a higher amount of organic compounds on the surface of the nanoparticles.

The EDS spectrum (Fig. 3) clearly shows signals corresponding to Fe, C, O, S, and N, confirming the successful synthesis of MFe_2O_4@PDA@$BuSO_3H$ MNPs, as the iron oxide nanoparticles are now functionalized with sulfonic acid groups. To assess the stability of the MFe_2O_4@PDA@$BuSO_3H$ and the bond formation between MFe_2O_4 and the organic agent, TGA was performed. The TGA curve (Fig. 4) shows an initial weight loss below 100 °C, which can be attributed to the desorption of solvent and surface hydroxyl groups. The subsequent weight loss is due to the decomposition of sulfonic acid grafted onto the surface of MFe_2O_4MNPs. The TGA curve indicates that the weight fraction of sulfonic acid is approximately 6.6%.

Surface morphology analysis of the synthesized nanocatalysts was conducted using SEM. The results revealed that the nanocatalysts exhibited a spherical shape, with an average size ranging from 40 to 50 nm (Fig. 5). TEM was employed to observe the particles, revealing their consistent size and shape. The particles exhibited a homogeneous size with an average diameter of 10 nm (Fig. 6).

To determine the optimal reaction conditions for synthesizing functionalized derivatives of 2-aminoimidazole-benzopyrazine hybrids, we conducted multicomponent domino reactions using benzopyrazine-2-carbaldehyde **1a** (1 mmol), aminoguanidine bicarbonate **2** (1 mmol) and ketones **3a**

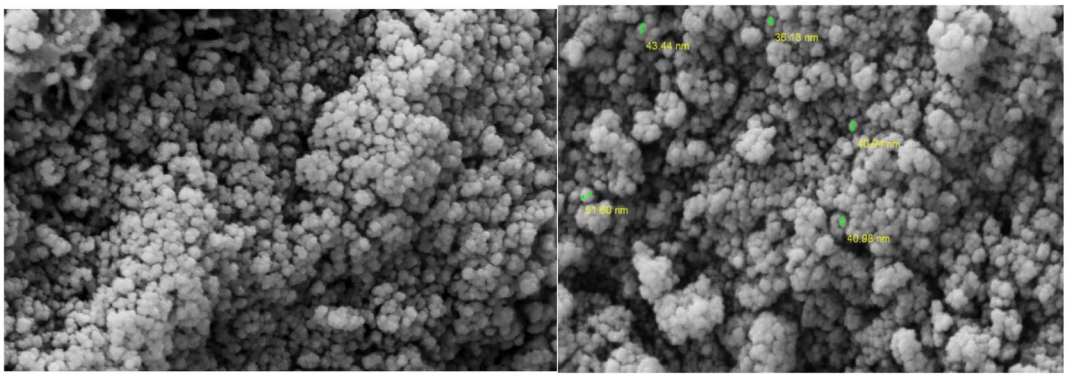

Fig. 5 SEM image of MFe_2O_4@DA@$BuSO_3H$.

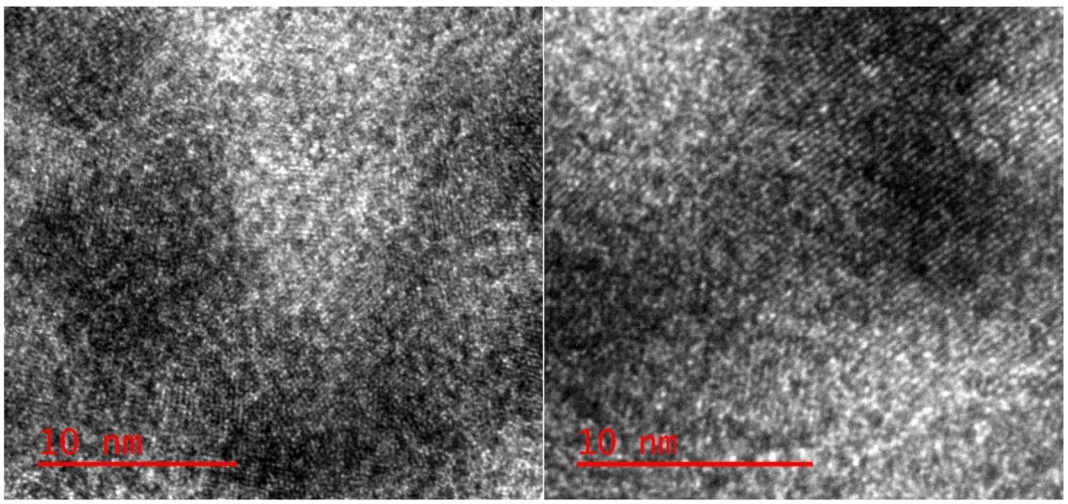

Fig. 6 TEM image of MFe_2O_4@PDA@ $BuSO_3H$.

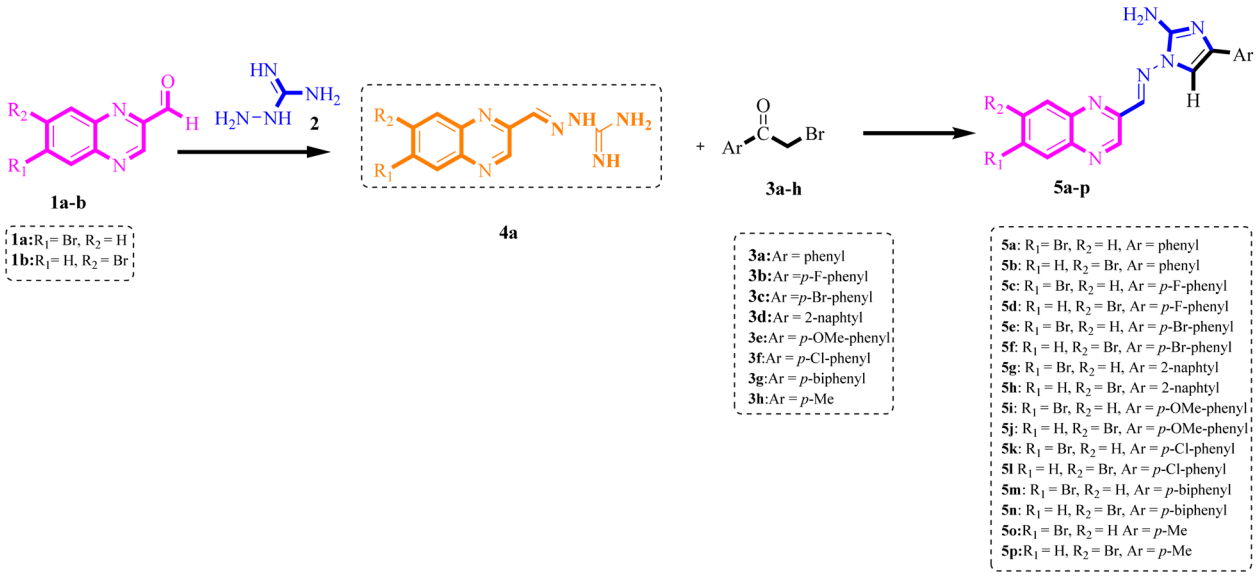

Scheme 2 Synthesis of functionalized benzopyrazine-aminoimidazole hybrid derivatives.

Table 1 Optimization of reaction conditions for compound **5a**

Entry	Catalyst (g)	Reaction conditions	Time (min)	Yield[a] (%)
1	—	EtOH, reflux	240	Nil
2	$BuSO_3H$ (0.005)	EtOH, reflux	120	70
3	MFe_2O_4 (0.03)	EtOH, reflux	160	40
4	MFe_2O_4@PDA (0.03)	EtOH, reflux	160	45
5	MFe_2O_4@PDA@SO_3H (0.05)	EtOH, reflux	120	87
6	MFe_2O_4@PDA@SO_3H (0.05)	H_2O, reflux	120	78
7	**MFe_2O_4@PDA@SO_3H (0.05)**	**H2O–EtOH (1 : 1), reflux**	**120**	**92**
8	MFe_2O_4@PDA@SO_3H (0.05)	H2O–EtOH (1 : 1), 50 °C	180	87
9	MFe_2O_4@PDA@SO_3H (0.07)	H2O–EtOH (1 : 1), 70 °C	120	92
10	MFe_2O_4@PDA@SO_3H (0.015)	H2O–EtOH (1 : 1), 70 °C	120	85

[a] Isolated yields.

as a model in ethanol (Scheme 2). Initially, we attempted the reaction in ethanol without a catalyst under reflux conditions for 4 hours (Table 1, entry 1). However, the desired product **5a** was not obtained, underscoring the necessity of catalytic assistance to drive the reaction and minimize the formation of by-products. When we refluxed **1a** and **2** in the presence of $BuSO_3H$ and ethanol, a brown solid of **4a** formed in less than 10 minutes. Subsequently, ethanol was used to heat the mixture under reflux conditions, and **3a** was added. $BuSO_3H$ (0.005 g) in ethanol led to the formation of **5a** with a yield of 70% (Table 1, entry 2), indicating moderate catalytic activity for the reaction. We further tested the effectiveness of different catalysts in the model reaction, including MFe_2O_4, MFe_2O_4@PDA, and MFe_2O_4@PDA@$BuSO_3H$; all were added in amounts below the stoichiometric ratio (0.05 g), and the reactions were conducted in ethanol under reflux conditions. After a thorough investigation, we established that MFe_2O_4@PDA@$BuSO_3H$ (0.05 g) demonstrated exceptional catalytic activity, resulting in short reaction times and high product yields. Specifically, MFe_2O_4 alone provided only a 40% yield (Table 1, entry 3), whereas modification with PDA slightly improved the yield to 45% (Table 1, entry 4). Notably, further functionalization with sulfonic acid groups (MFe_2O_4@PDA@SO_3H) significantly enhanced the yield to 87% (Table 1, entry 5), illustrating the crucial role of the acidic groups in catalysis. Additionally, we investigated various solvents for the synthesis of compound **5a**. Individual solvents did not yield efficient results. However, when the reaction was carried out in a mixture of ethanol and water (1 : 1), robust hydrogen bonding ability and a high degree of polarity resulted in increased yields within reduced reaction times. Adhering to the principles of green chemistry, we did not test any other organic solvents in this experiment. After thorough screening, it was determined that the optimal yields and time profiles were achieved by conducting the reaction with 0.05 g of MFe_2O_4@PDA@$BuSO_3H$ MNPs in a mixture of ethanol and water (1 : 1) under reflux conditions. This resulted in the formation of the corresponding **5a** with a yield of 92% in 2 hours (Table 1, entry 7). Further analysis on the effect of temperature variation

revealed that lowering the reaction temperature to 50 °C in the H_2O–EtOH system reduced the yield to 87%, despite a prolonged reaction time (Table 1, entry 8). Increasing the catalyst amount to 0.07 g did not further improve the yield beyond what was achieved with 0.05 g (Table 1, entry 9). Conversely, reducing the catalyst amount to 0.015 g slightly decreased the yield to 85% (Table 1, entry 10).

To generate a limited collection of functionalized derivatives of 2-aminoimidazole benzopyrazine hybrids (**5a–p**), we employed various substrates to investigate the extent and versatility of the accelerated *via* a single-step, one-pot Knoevenagel-shift base-annulation reaction under optimized conditions. The outcomes of this exploration are summarized in Table 2. These novel compounds were identified through elemental analysis and spectral characterization, including ^{1}H NMR, ^{13}C NMR, 2D NMR (HHCOSY and HMBC), mass spectrometry (MS) and infrared (IR) spectroscopy. The mass spectra showed peaks at the expected *m*/*z* values for the molecular ions.

Subsequently, we applied the optimal reaction parameters to examine the reaction's effectiveness for synthesizing 2-aminoimidazole-containing benzopyrazine derivatives. Various 2-bromoacetophenones with different substituents were converted to the desired products with high yields using MFe_2O_4@PDA@$BuSO_3H$ MNPs as a green catalyst. Notably, electron-withdrawing groups on the 2-bromo acetophenone derivatives facilitated the reactions, reducing reaction times and increasing yields compared to electron-releasing groups on the benzene ring.

The recoverability and reusability of catalysts are significant benefits of the green chemistry approach using heterogeneous catalysts, particularly from an industrial standpoint for operations on commercial-scale applications. Accordingly, we investigated the recycling of fresh MNPs using a selected model reaction involving compounds **1a**, **2**, and **3a** in the presence of MFe_2O_4@PDA@$BuSO_3H$ (Table 2, entry 1). After the reaction (monitored by TLC) was completed, a hot ethanol dilution was

Table 2 MFe_2O_4@PDA@$BuSO_3H$ (0.05 g) as catalyzed multi-component domino reactions for the one-pot efficient synthesis of benzopyrazine derivatives containing 2-aminoimidazole

Entry	R_1	R_2	Ar	Compound	Time (h)	Mp (°C)	Yield %
1	Br	H	Phenyl	**5a**	3	251–253	87
2	H	Br	Phenyl	**5b**	3	252–254	85
3	Br	H	*p*-F-phenyl	**5c**	2	250–253	90
4	H	Br	*p*-F-phenyl	**5d**	3	254–257	89
5	Br	H	*p*-Br-phenyl	**5e**	2	255–258	90
6	H	Br	*p*-Br-phenyl	**5f**	3	257–259	89
7	Br	H	2-Naphtyl	**5g**	3	274–276	88
8	H	Br	2-Naphtyl	**5h**	2	273–276	87
9	Br	H	*p*-OMe-phenyl	**5i**	3	243–246	89
10	H	Br	*p*-OMe-phenyl	**5j**	2	241–243	88
11	Br	H	p-Cl-phenyl	**5k**	2	238–240	89
12	H	Br	p-Cl-phenyl	**5l**	2	238–240	87
13	Br	H	p-biphenyl	**5m**	2	257–260	85
14	H	Br	p-biphenyl	**5n**	2	258–260	84
15	Br	H	*p*-Me	**5o**	3	247–249	84
16	H	Br	*p*-Me	**5p**	3	230–232	82

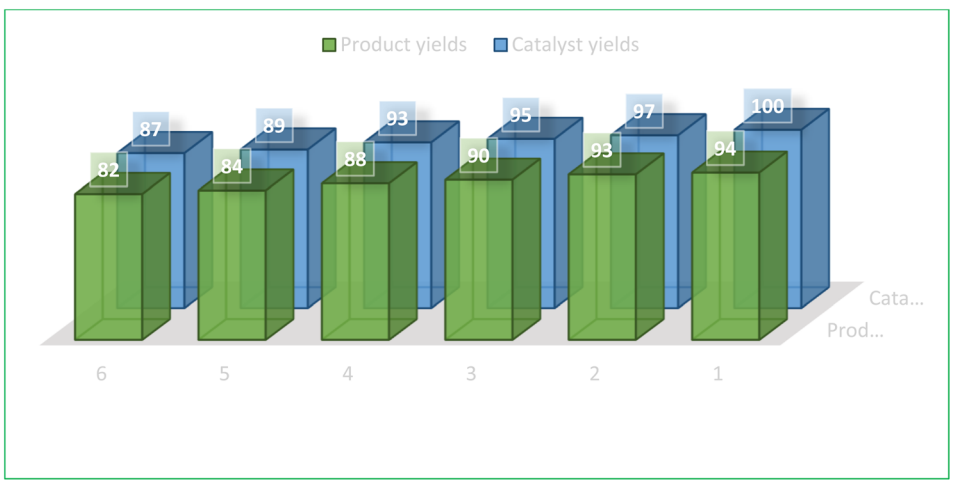

Fig. 7 Reusability of nanocatalyst.

performed to facilitate the separation of the catalyst from the reaction mixture. The catalyst was then quickly removed using an external magnetic field. The catalyst was then washed with hot ethanol, dried in ambient air, and utilized again for subsequent similar reactions. Notably, the catalyst retained its ability to catalyze reactions for six cycles without appreciable performance diminution (Fig. 7).

Scheme 3 illustrates one of the proposed reaction pathways for the one-pot multicomponent Knoevenagel-shift base reactions using MFe_2O_4@PDA@$BuSO_3H$ MNPs as a heterogeneous Lewis acid catalyst. Although the precise mechanism is not fully understood, it is hypothesized that the surface of the MFe_2O_4@PDA@$BuSO_3H$ MNPs heterogeneous nanocatalyst possesses electron-deficient sites capable of coordinating with the O-donor sites of aldehyde and (substituted) bromoacetophenone. This coordination, especially with the empty orbital of the $-SO_3H$ group on the functionalized MFe_2O_4surface, enhances the electrophilicity of the carbonyl carbon atoms in both formaldehyde and bromoacetophenone. Consequently, the one-pot multicomponent Knoevenagel-shift base reactions efficiently proceed, leading to the formation of the corresponding Knoevenagel-shift base product. In the initial step of this reaction: **I.** Activation of the nano catalyst's surface through coordination with the $-SO_3H$ group; **II.** Electrophilic attack on the carbonyl carbon atom of formaldehyde by the activated catalyst; **III.** Formation of a transient intermediate complex between the nano catalyst and the carbonyl compound; **IV.** Nucleophilic attack by the amine group of the guanidine compound on the carbonyl carbon atom, facilitated by coordination with the nano catalyst; **V.** Formation of an imine intermediate through the reaction between the carbonyl compound and the guanidine compound; **VI.** Release of the imine intermediate from the nano catalyst's surface; **VII.** Formation of an imine intermediate through nucleophilic attack by aminoguanidine on the carbonyl carbon atom in the aldehyde; **VIII.** Intramolecular proton transfer and rearrangement of bonds occur, resulting in the formation of an imine intermediate; **XI.** Interaction between the bromoacetophenone derivative and the imine compound leads to the formation of the aminoimidazole ring and the final derivatives; **X.** In the formation of the final derivative, two moles of imine compounds are required for each mole of alpha-bromo compound; **XI.** The initial step involves the formation of an imine intermediate between the carbonyl group of the alpha-bromo compound and the imine group; **XII.** With the entry of the next imine compound, the imidazole ring is formed; **XIII.** Finally, one extra mole of imine compound is expelled, forming the desired final derivative.

This heterogeneous nanocatalyst is functionalized with $-SO_3H$ groups, providing Lewis acid sites on its surface.[17–19] These acidic centers coordinate with electron-donating groups such as the oxygen in the carbonyl compounds, namely the aldehyde and bromoacetophenone utilized in this reaction. Upon coordination, the catalyst enhances the electrophilicity of the carbonyl carbon atoms, making them more susceptible to nucleophilic attack. The nanocatalyst acts as an electron-withdrawing entity, stabilizing the negative charge on the intermediates formed during the reaction. This stabilization

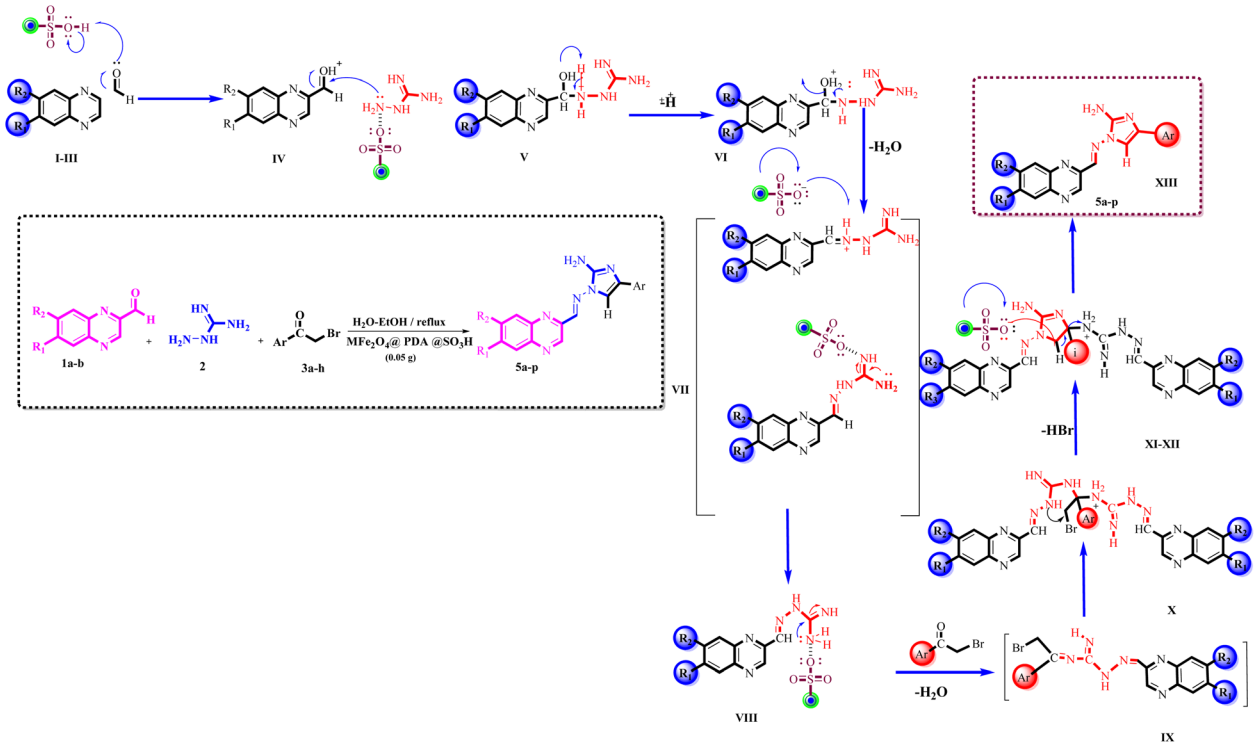

Scheme 3 The proposed mechanism for preparing 2-benzopyrazine-aminoimidazole hybrid derivatives (**5a–p**) using MFe_2O_4@PDA@$BuSO_3H$ MNPs (0.05 g) as catalyst in H_2O–EtOH (1 : 1), reflux.

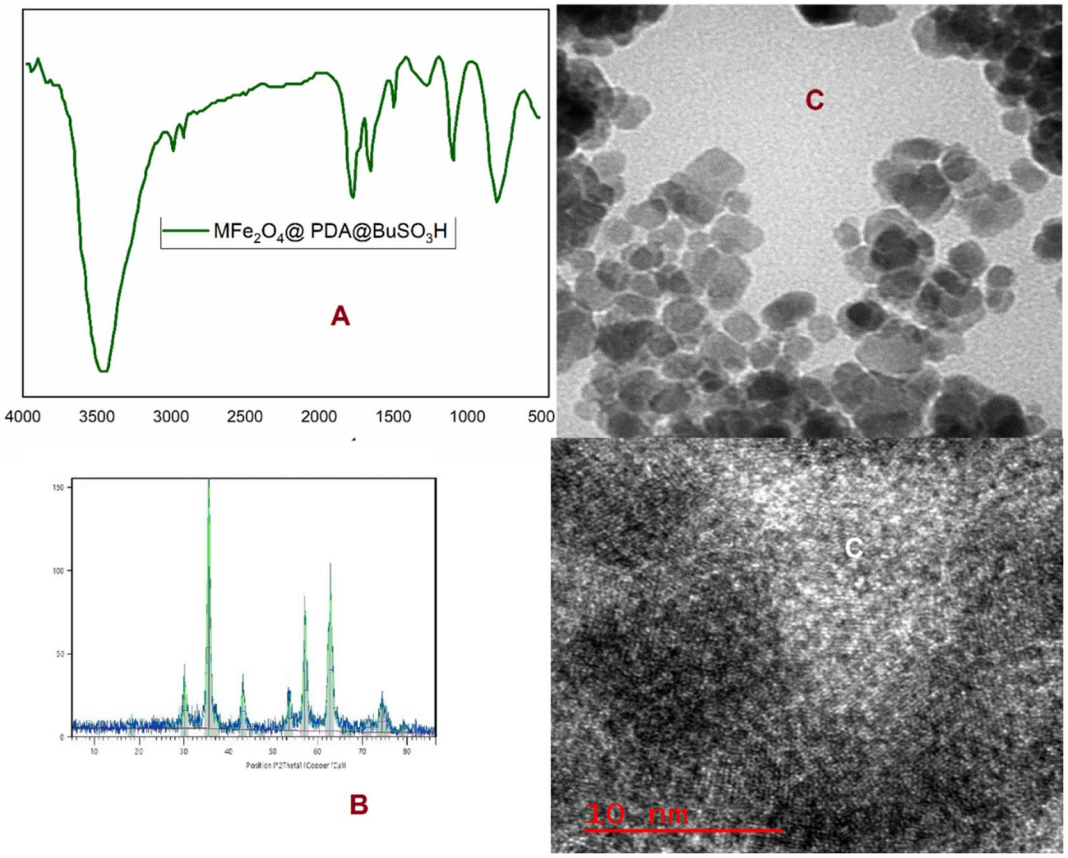

Fig. 8 A) FT-IR, (B) XRD, and (C) TEM analysis of the recovered MFe_2O_4@PDA@$BuSO_3H$ MNPs (0.05 g) as a catalyst in H_2O–EtOH (1 : 1), reflux.

lowers the activation energy required, thus accelerating the reaction process. Moreover, the catalyst facilitates the correct orientation of reactants, which is critical for forming the imine. The amine group of the guanidine compound is positioned in close proximity to the activated carbonyl compound, promoting a more efficient nucleophilic attack to form the imine intermediate. Additionally, the catalyst provides a surface that can adsorb and desorb the reactants and products, optimizing the transformation and release of the desired product. Once the product is formed, it detaches from the catalyst, allowing the catalyst to participate in another catalytic cycle without any permanent structural changes. The entire process benefits from the catalyst's involvement, encompassing sequential steps of activation, intermediate formation, nucleophilic attack, and the eventual creation and release of the final product, all facilitated and accelerated by the catalytic activity of MFe_2O_4@PDA@$BuSO_3H$ MNPs.

The stability of the MFe_2O_4@PDA@$BuSO_3H$ MNPs was demonstrated through multiple catalytic cycles involving the synthesis of benzopyrazine-aminoimidazole hybrids. After each reaction cycle, the nanocatalyst was magnetically separated, washed, and reused. The catalytic activity remained consistent even after six cycles. Structural characterization was conducted using FT-IR and XRD analyses before and after repeated catalytic cycles to assess any structural changes. The spectra and diffraction patterns exhibited no significant alterations, indicating the structural integrity of the nanocatalyst (Fig. 8A and B). TEM observed the morphological stability of the nanocatalyst. The images confirmed that the core–shell structure was retained after repeated catalytic cycles, further substantiating the stability claim (Fig. 8C). In terms of greenness, the synthesis of the nanocatalyst and the catalytic reactions occurred under mild reaction conditions using environmentally friendly solvents such as ethanol or water at ambient or relatively low temperatures. This approach significantly reduces the environmental footprint.

2.1.2. Hot filtration test. During the experimental procedure, the magnetically responsive nanoparticles that were the driving force of the catalysis in the reaction mixture were magnetically separated after 50 minutes. Following this separation, observation revealed a cessation in reaction progress, underscoring that all catalytically active MNPs had been effectively removed without leaving behind any active species in the solution. This outcome supports the conclusion that the catalysis operated on a heterogeneous basis with a stable catalyst framework and without the loss of SO_3H functionalities. Furthermore, the acidic SO_3H sites on the catalyst's surface were quantified using back titration with a 0.01 mol L^{-1} KOH solution. The analysis confirmed the presence of 1.4 millimoles of SO_3H groups per gram of the catalyst, composed of an MFe_2O_4 core encased within a PDA layer functionalized with $BuSO_3H$.

Table 3 *In vitro* antiproliferative activities of the target compounds 5a–p

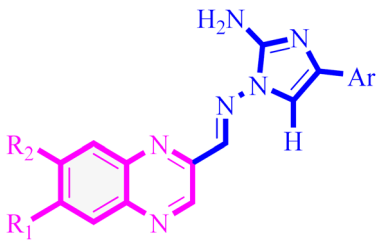

(5a-p)

Compound	R_1	R_2	Ar	IC_{50} (μM) MCF7	SKOV3	U87
5a	Br	H	Phenyl	1.90	1.38	1.08
5b	H	Br	Phenyl	1.11	2.99	2.00
5c	Br	H	*p*-F-phenyl	2.44	2.35	2.60
5d	H	Br	*p*-F-phenyl	1.84	1.98	6.61
5e	Br	H	*p*-Br-phenyl	3.82	3.06	2.83
5f	H	Br	*p*-Br-phenyl	1.86	4.36	2.24
5g	Br	H	2-Naphtyl	0.03	1.22	0.22
5h	H	Br	2-Naphtyl	0.32	0.51	0.93
5i	Br	H	*p*-OMe-phenyl	2.02	1.84	4.23
5j	H	Br	*p*-OMe-phenyl	1.56	1.78	1.28
5k	Br	H	*p*-Cl-phenyl	1.40	1.63	1.97
5l	H	Br	*p*-Cl-phenyl	3.22	1.13	1.56
5m	Br	H	*p*-Biphenyl	1.65	19.8	2.38
5n	H	Br	*p*-Biphenyl	0.11	1.93	1.97
5o	H	Br	*p*-Me	4.08	2.16	2.84
5p	Br	H	*p*-Me	2.29	2.01	2.11
Doxorubicin				0.50	1.76	0.31

2.2. Biological evaluation

2.2.1. Antiproliferative evaluation. The efficacy of newly prepared compounds against three cancerous cell lines including A549 (human lung adenocarcinoma epithelial cell line), MCF7 (breast cancer), U87 (glioblastoma cell line), was evaluated through *in vitro* MTT (3-(4,5-dimethylthiazol-2-yl)-2,5-diphenyltetrazolium bromide) assay, following established literature methods.[21,22] Doxorubicin was used as the standard drug for comparison. The cytotoxicity of each compound against the different cancer cell lines was assessed by determining the concentration (μM) required to inhibit 50% of cell growth, known as the IC_{50} (Half Maximal Inhibitory Concentration) value, as presented in Table 3. Previous findings have suggested that incorporating a substituent at the C4 position of the C-ring (imidazole) could enhance compounds' growth inhibitory effects in a laboratory setting and their ability to dissolve in water. Hence, our investigation aimed to improve the water solubility and discover more potent anticancer compounds by attaching various functional groups to the C4 position of the C-ring. The data presented in Table 3 reveal that most compounds demonstrated remarkable anticancer effects against the three human cell lines at concentrations below one micromolar, with IC_{50} values of 0.03 to 19.8 μM. The correlation between the chemical structure of compounds **5a–p** and their biological activity was further analyzed based on the initial MTT screening results. Initially, we introduced a phenyl or p-substituted phenyl ring at the C4 position of the C-ring. Upon modification of the A-ring substituent was either hydrogen or an electron-withdrawing group like Bromo, the antiproliferative activities of the compounds were not significantly different (IC_{50} = 1.11–6.61 μM). Similarly, when a biphenyl moiety was introduced at the C4 position of the C-ring, compounds **5m** and **5n** did not exhibit potent antiproliferative activity. Surprisingly, when a 2-naphthyl ring was used as the C4 substituent of the C-ring, the activity significantly improved for compounds **5g** and **5h**, with IC_{50} values of 0.03 and 0.32 μM, respectively, against MCF-7 cells. Furthermore, inserting a bromo substituent (compound **5g**) at the C3 position of the A-ring enhanced the inhibitory activities against all three cancer cell lines. In summary, derivatives with a 2-naphthyl ring at the C4 position of the C-ring exhibited superior antiproliferative activity compared to those with a phenyl or *p*-substituted phenyl ring, biphenyl ring, or *para*-methyl group. Additionally, including a bromo group at the C3 position of the A-ring further enhanced the anticancer activity. Given its favorable antiproliferative activity in a laboratory setting, compound **5g** was chosen as the most promising candidate for further preclinical development.

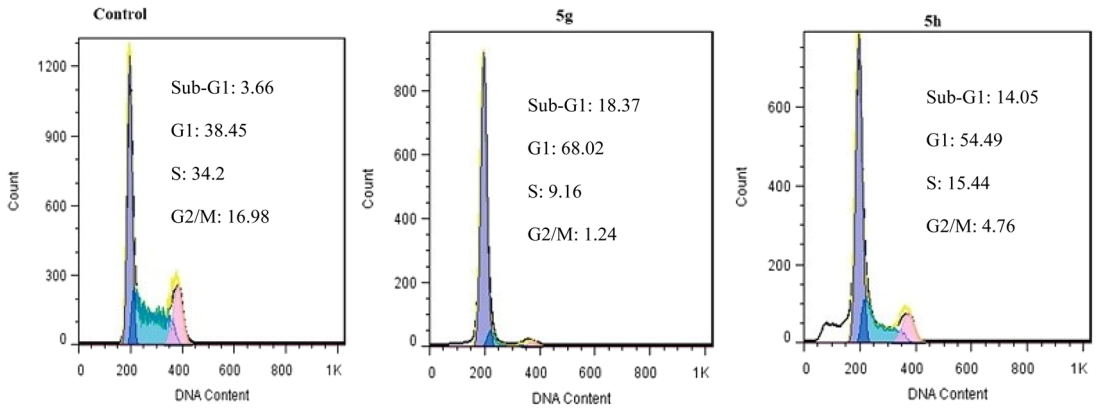

Fig. 9 Cell cycle assay.

2.2.2. Cell cycle arrest induced by 5g and 5h. Compounds **5g** and **5h** were chosen as the prominent derivatives for flow cytometric cell cycle experiments on MCF-7 cells to evaluate antiproliferative effects further. After 48 h exposure of MCF-7 cells, the data was obtained with 3 μM of compounds **5g** and **5h** using propidium iodide (PI), and the untreated cells were introduced as the negative control. As shown in Fig. 9, compounds **5g** and **5h** strongly affected the sub-G1 phase. After cell treatment by representative compounds **5g** and **5h**, cell population percentage in the sub-G1 phase remarkably increased from 3.66% to 18.37% and 14.05%, respectively, compared to the control experiment. Furthermore, the rise in the number of cells in the G1 phase after treatment by **5g** and **5h**, from 38.45% to 68.02% and 54.49%, was demonstrated in Fig. 9. The experimental outcomes were responsible for the decline in the proportion of cells in the G2/M phase, which consequently led to the arrest of the cell cycle in the G1 and S phases.

2.2.3. Cell apoptosis induced by 5g and 5h. The results obtained from the cell cycle analysis indicate a significant increase in the sub-G1 phase in MCF-7 cells treated with representative compounds, which is typically associated with cell apoptosis. To evaluate the potential of compounds **5g** and **5h** to induce cell death in the MCF-7 cell line *via* apoptosis, we conducted an Annexin staining assay at 1.5 and 3 μM for 48 h. As shown in Fig. 10, the ability of compounds **5g** and **5h** to induce apoptosis at both early and late stages was demonstrated in a time and dose-dependent manner, compared to untreated cells. Subsequently, the value of apoptosis-induced cells in the presence of 1.5 and 3 μM of compounds **5g** and **5h** increased from 18.61% and 13.6% to 29.27% and 16.92%, respectively.

2.3. Molecular docking study

Molecular docking simulations were conducted on the most potent compounds. The docking investigation demonstrated that promising compounds **5g** and **5h** colchicine binds with high affinity to the β-subunit of tubulin. Forming essential hydrogen bonds, van der Waals interactions, and polar interactions are responsible for stabilizing the obtained interaction mode. Docking modes shown in Fig. 11A and Fig. 11C demonstrate that the benzopyrazine moiety in compound **5g** was interred in the hydrophobic pocket of the colchicine

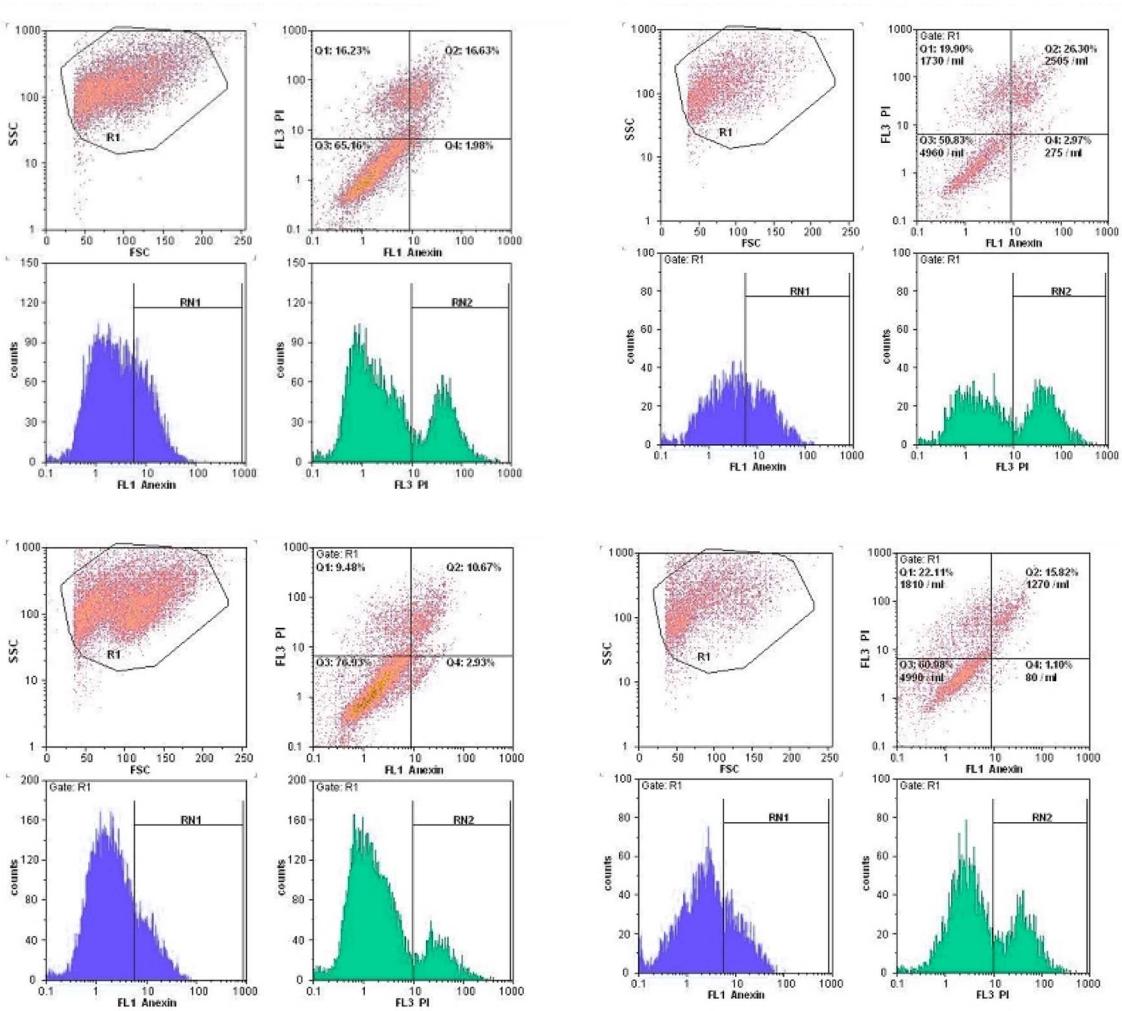

Fig. 10 Compounds **5g** and **5h** induced apoptosis in MCF-7 cells. 1.5 and 3 μM for 48 h.

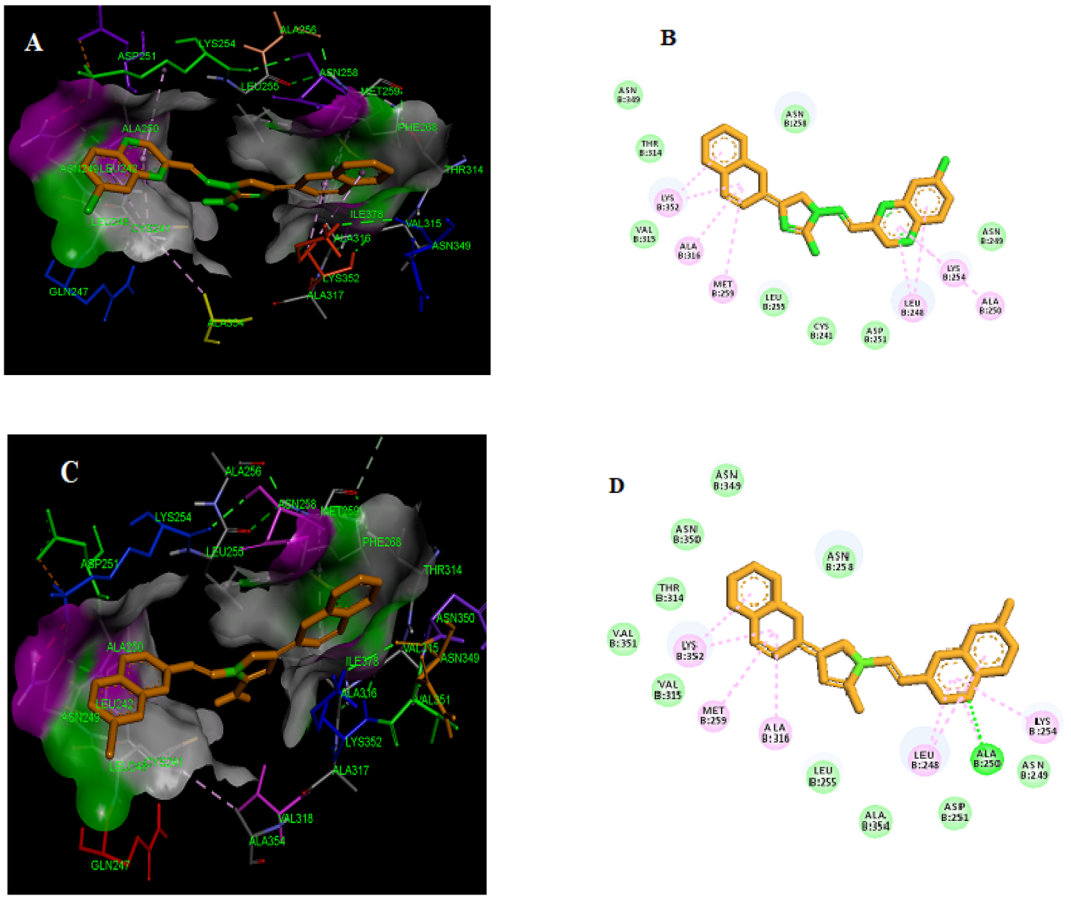

Fig. 11 Compounds **5g** (A and B) and **5h** (C and D) are both potent tubulin polymerization inhibitors that bind to the colchicine binding site.

binding site in the β-tubulin and is in contact with amino acids such as βAla250, βLys254, βLeu248, βAsn249. The imidazole ring is buried in the amino acid residues, including βLeu255, βCys241, and βAsp251. Similarly, the 2D representation of compound **5g** displayed several secondary interactions like van der Waal interactions with the residues of βAsn258, βAsn349, βAsn249, βThr314, βVal315, βAsp251, βLeu255 and βCys241. Besides this, the formation a pi-alkyl interaction between the 3,4,5-trimethoxyphenyl moiety and βLeu255 and a pi-alkyl interaction between benzopyrazine ring and amino acid residues βAla250, βLys254, βLus248 and between bipheyl ring with the residues of βAla316, βLys352 and, βMet259 were detected, respectively. The molecular docking results for compound **5h** (Fig. 11B) showed that the benzopyrazine moiety is encircled by the amino acid residues βLys254, βAla250, βLeu248, and βAsn249. The amino acid residues βAla354, βAsn258, and βLeu255 surrounded the imidazole ring.

Furthermore, 2D presentation of the binding interaction mode of compound **5h** (Fig. 11D) demonstrates the formation of two pi-alkyl interactions between the benzopyrazine scaffold and βLeu248 and βLys254 and three pi-alkyl interaction between biphenyl ring and βAla316, βLys352, and βMet259. Moreover, several van der Waal interactions between the benzopyrazine ring and biphenyl ring with amino acid residues βAsn249, βAla354, βAsp251, βVal351, βThr314, βAsn350, βAsn349, and βAsn258 were detected. Besides, the formation of a conventional hydrogen bond between benzopyrazine moiety and the amino acid residue of βAla250 was shown.

3. Conclusion

We have reported a novel and efficient acidic nanocatalyst (MFe_2O_4@PDA@$BuSO_3H$) through single-pot domino Knoevenagel-shift base–annulation reactions, which possess magnetic properties and can overcome the limitations of traditional mineral or homogeneous organic catalysts. MFe_2O_4@PDA@$BuSO_3H$ MNPs is an environmentally friendly, cost-effective, and magnetic nanocatalyst that can be quickly recovered using a simple magnet and reused multiple times without significantly reducing its catalytic performance. We have synthesized aminoimidazole hybrids benzopyrazine derivatives in this nanocatalyst's presence, after which their anti-proliferative effects against three human cancer cell lines, namely MCF-7, U87, and A549, were evaluated. All tested derivatives (**5a–p**) exhibited significant cytotoxic activity. Compound **5g**, which possesses a 2-naphthyl ring at the C4 substituent of the C-ring, demonstrated the highest cytotoxicity among other derivatives with IC_{50} values of 0.03 μM, which were 17-fold more potent than the standard drug doxorubicin. Furthermore, our cell cycle analysis revealed that the disruption

caused by compounds **5g** and **5h** significantly affected microtubule polymerization and resulted in the significant arrest of most MCF7 cells in the G2/M phase.

Through our Molecular Docking analysis, we gained insights into the precise binding site of compounds **5g** and **5h** with tubulin. Moreover, we confirmed that the interaction between these compounds and the colchicine binding site of tubulin is responsible for their anti-proliferative activity.

4. Experimental section

4.1 Chemistry

4.1.1. Synthesis of MFe_2O_4@PDA@$BuSO_3H$ MNPs. This study synthesized magnetite nanoparticles *via* the co-precipitation method.[18,19] Using ultrasound, the resulting nanoparticles were dispersed in 500 mL of Tris (hydroxymethyl) aminomethane buffer at a pH of 8.5 and 10 mmol L^{-1} concentration. Dopamine hydrochloride (1 g) was added to the dispersion, and the mixture was stirred continuously for 6 hours. The nanoparticles were then collected using an external magnet and rinsed several times with deionized water. The solid obtained was mixed with 25 mL of dry toluene and subjected to sonication for 1 hour. 1 $BuSO_3H$ (5 mL) was added to the colloidal solution, and the mixture was refluxed for 10 hours. The nanomagnetic catalyst was then separated by an external magnet and washed with dichloromethane before drying at room temperature.

4.1.2. General procedure for the synthesis of new aminoimidazole-benzopyrazine derivative. 1 mmol of compounds **1a–c**, 1 mmol of compound **2**, 0.03 g of MFe_2O_4@PDA@$BuSO_3H$, and 30 mL of a 1 : 1 v/v mixture of H_2O and EtOH were combined in a 50 mL flask fitted while stirring with a magnetic stirrer at 70 °C for less than 10 minutes. Then,1 mmol of cyclic ketones **3a–h** was added to the flask, and the reaction was heated for the times specified in Table 2. After the reaction was completed, as determined by TLC analysis, hot Ethanol was afforded to the reaction mixture, followed by the catalyst's separation using an external magnet. The catalyst was then washed with hot ethanol, dried, and reused for a consecutive run with the same set of conditions. The reaction mixture was cooled after the completion of the reaction, and the unrefined compound was isolated by filtration. To ensure the highest purity of the product, the raw compound was first subjected to column chromatography using an appropriate solvent system to achieve preliminary purification. Following this step, preparative thin-layer chromatography (TLC) was performed for the final purification of the compound. The purified product was then recrystallized from hot ethanol to obtain the final pure compound.

4.2. Biological tests

4.2.1. Cytotoxicity evaluation. The study utilized several cancer cell lines, namely A549, U87, and. MCF7. These cells were maintained in DMEM High Glucose from Atocell, supplemented with 10% fetal bovine serum (FBS) and 1% antibiotics penicillin (50 U per mL) and streptomycin (50 μg mL^{-1}) from Sigma-Aldrich. They were kept at 37 °C with 5% CO_2. When these cells reached 50–70% confluence, they were detached using 0.2% trypsin–EDTA and then placed into 96-well plates at 1×10^4 cells per well density. Each well had 200 μL of cell suspension, and the plates were then incubated at 37 °C with 5% CO_2 for 48 hours to create a monolayer culture. After 48 hours, the old medium from each well was removed, and the test compounds were added at concentrations of 1, 5, 10, 20, 50, and 100 μg mL^{-1} to a 96-well plate. Both positive control (doxorubicin) and negative control (vehicle) groups were included, and the experiments were repeated three times. Then, cells were incubated for 48 hours at 37 °C with 5% CO_2. The MTT assay was used to obtain cell viability. In each well, 10 μL of MTT solution was added, and the cells were incubated for 4 hours at 37 °C. After discarding the supernatant, 200 μL of DMSO was added. Then, the optical density was determined at a wavelength of 570 nm. Concentration *versus* cell viability (%) curves were plotted, and the IC_{50} amounts were determined using GraphPad Prism software (version 6).[23]

4.2.2. Cell cycle assay. To evaluate the effect of **5g** and **5h** compounds on the cell cycle arrest of MCF-7 cells, we grew 2.5 mL samples containing 1.0 × 105 cells per mL in 6-well plates. The plates were incubated at 37 °C for 24 hours in a CO_2 incubator with 5% CO_2.[24] The propidium iodide staining assay from Sigma was employed to arrest the cell cycle of MCF-7 cells, following established protocols. Subsequently, cells were exposed to compounds **5g** and **5h** at concentrations of 2 μM for 48 hours. After the treatment, the cells were centrifuged, fixed with 70% ethanol at 4 °C overnight, and then resuspended in phosphate-buffered saline solution containing 100 μL RNase A and 400 μL propidium iodide. Analysis of cell cycle distribution was performed by collecting twenty thousand events per sample using a FACS Calibur flow cytometer from BD Biosciences.[25]

4.2.3. Annexin V-FITC analysis for apoptosis. The present study evaluated the induction of apoptotic cell death through flow cytometry analysis using Annexin V and propidium iodide.[26] The MCF-7 cells were seeded at a density of 1×10^5 cells per mL in 6-well plates and exposed to either vehicle (0.1% (v/v) EtOH) or compound **5g** and **5h** at 2.5 and 5 μM for 48 hours. After that, cells were treated with trypsin, washed with cold PBS, and centrifuged at 3000 rpm. The cells were subsequently mixed with Annexin-V in a binding buffer at room temperature for 15 minutes, With the addition of propidium iodide solution. Flow cytometric analysis was performed using a FAC Scan, and the number of cells was determined based on emission and excitation using 488 nm and 535 nm for Annexin-V/FITC and 488 nm and 610 nm for PI.

4.3. Docking simulations

The mode of interaction between promising compounds **5g** and **5h** with the colchicine binding site of tubulin was examined by employing AutoDock software to investigate the structural basis of the aforementioned biological findings. The structure of compounds was drawn in ChemDraw, and 3D structures were prepared in ChemBioDraw Ultra16.0, following energy minimization using the MM2 force field. The crystal structure of

tubulin complexed with colchicine was obtained from the PDB database (PDB code 1SA0). Using the AutoDock protocol,[27] final files were prepared. A grid box of 45, 45, and 45 grid points (X, Y, Z dimensions, resp.) and centroid: $X = 117.2187$, $Y = 90.1800$, $Z = 6.2898$ was chosen. The obtained interactions and poses were analyzed, and exhibiting optimal ligand-enzyme interactions were chosen and saved for energy calculations.

Data availability

All data generated or analyzed during this study are included in this published article and data will be made available on request.

Conflicts of interest

There are no conflicts to declare.

Acknowledgements

The authors extend their appreciation to the Deputyship for Research & Innovation, Ministry of Education in Saudi Arabia, for funding this research work through the project number (PSAU/2023/R/1444). This study is supported *via* funding from the Prince Sattam Bin Abdulaziz University project number (PSAU/2023/R/1444).

References

1 J. Lin, P. Wang, Z. Zhang, G. Xue, D. Zha, J. Wang, X. Xu and Z. Li, *Synth. Commun.*, 2020, **50**, 823–830.
2 E. A. Fayed, Y. A. Ammar, M. A. Saleh, A. H. Bayoumi, A. Belal, A. B. Mehany and A. Ragab, *J. Mol. Struct.*, 2021, **1236**, 130317.
3 M. Ibrahim, M. Taghour, A. Metwaly, A. Belal, A. Mehany, M. Elhendawy, M. Radwan, A. Yassin, N. El-Deeb and E. Hafez, *Eur. J. Med. Chem.*, 2018, **155**, 117–134.
4 M. Montana, F. Mathias, T. Terme and P. Vanelle, *Eur. J. Med. Chem.*, 2019, **163**, 136–147.
5 M. M. Alanazi, H. Elkady, N. A. Alsaif, A. J. Obaidullah, W. A. Alanazi, A. M. Al-Hossaini, M. A. Alharbi, I. H. Eissa and M. A. Dahab, *J. Mol. Struct.*, 2022, **1253**, 132220.
6 N. A. Alsaif, A. Elwan, M. M. Alanazi, A. J. Obaidullah, W. A. Alanazi, A. F. Alasmari, H. Albassam, H. A. Mahdy and M. S. Taghour, *Mol. Diversity*, 2022, **26**, 1915–1932.
7 D. S. Ermolat'ev, J. B. Bariwal, H. P. Steenackers, S. C. De Keersmaecker and E. V. Van der Eycken, *Angew. Chem.*, 2010, **122**, 9655–9658.
8 M. MATSUyAMA, K. Funao, K. Kuratsukuri, T. Tanaka, Y. Kawahito, H. Sano, J. Chargui, J.-L. Touraine, N. Yoshimura and R. Yoshimura, *Exp. Ther. Med.*, 2010, **1**, 301–306.
9 T.-C. Shih, R. Liu, C.-T. Wu, X. Li, W. Xiao, X. Deng, S. Kiss, T. Wang, X.-J. Chen and R. Carney, *Clin. Cancer Res.*, 2018, **24**, 4319–4331.
10 T.-C. Shih, R. Liu, G. Fung, G. Bhardwaj, P. M. Ghosh and K. S. Lam, *Mol. Cancer Ther.*, 2017, **16**, 1212–1223.
11 S. Reyes, R. W. Huigens III, Z. Su, M. L. Simon and C. Melander, *Org. Biomol. Chem.*, 2011, **9**, 3041–3049.
12 H. Weinmann, M. Harre, K. Koenig, E. Merten and U. Tilstam, *Tetrahedron Lett.*, 2002, **43**, 593–595.
13 M. Akhavan and A. Bekhradnia, *RSC Adv.*, 2021, **11**, 14755–14768.
14 M. Akhavan, N. Foroughifar, H. Pasdar and A. Bekhradnia, *Combinatorial Chemistry & High Throughput Screening*, 2019, 22, 716–727.
15 F. Sahin, E. Turan, H. Tumturk and G. Demirel, *Analyst*, 2012, **137**, 5654–5658.
16 Z. Esam, M. Akhavan, A. Bekhradnia, M. Mohammadi and S. Tourani, *Catal. Lett.*, 2020, **150**, 3112–3131.
17 Z. Esam, M. Akhavan, A. Mirshafa and A. Bekhradnia, *RSC Adv.*, 2023, **13**, 25229–25245.
18 M. Akhavan, Z. Esam, A. Mirshafa, M. Lotfi, S. Pourmand, F. Ashori, M. Rabani, G. Ekbatani, S. Tourani and R. Beheshti, *RSC Adv.*, 2024, **14**, 22916–22938.
19 Z. Kheilkordi, G. M. Ziarani and A. Badiei, *Polyhedron*, 2020, **178**, 114343.
20 P. Diana, A. Martorana, P. Barraja, A. Montalbano, G. Dattolo, G. Cirrincione, F. Dall'Acqua, A. Salvador, D. Vedaldi and G. Basso, *J. Med. Chem.*, 2008, **51**, 2387–2399.
21 T. Liang, X. Zhou, L. Lu, H. Dong, Y. Zhang, Y. Xu, J. Qi, Y. Zhang and J. Wang, *Bioorg. Chem.*, 2021, **110**, 104793.
22 M. Akhavan, N. Foroughifar, H. Pasdar, A. Khajeh-Amiri and A. Bekhradnia, *Transition Met. Chem.*, 2017, **42**, 543–552.
23 L. Deferme, J. Briede, S. Claessen, D. Jennen, R. Cavill and J. Kleinjans, *Toxicology*, 2013, **306**, 24–34.
24 L. Browne, C. Gude, H. Rodriguez, R. Steele and A. Bhatnager, *J. Med. Chem.*, 1991, **34**, 725–736.
25 Y. Koizumi, M. Arai, H. Tomoda and S. Ōmura, *Biochim. Biophys. Acta*, 2004, **1693**, 47–55.
26 S. Forli, R. Huey, M. E. Pique, M. F. Sanner, D. S. Goodsell and A. J. Olson, *Nat. Protoc.*, 2016, **11**, 905–919.
27 S. M. D. Rizvi, S. Shakil and M. Haneef, *EXCLI J.*, 2013, **12**, 831.